Journal of African Earth Sciences 123 (2016) 392–402

Contents lists available at ScienceDirect

Journal of African Earth Sciences

journal homepage: www.elsevier.com/locate/jafrearsci

Mineral chemistry and petrology of mantle peridotites from the Guleman ophiolite (SE Anatolia, Turkey): Evidence of a forearc setting

Mustafa Eren Rizeli [a], Melahat Beyarslan [a, *], Kuo-Lung Wang [b], A. Feyzi Bingöl [a]

[a] Department of Geological Engineering, Firat University, TR-23119 Elazig, Turkey
[b] Academia Sinica Institute of Earth Sciences, 128 Academia Road Section 2, Taipei 115, Taiwan

ARTICLE INFO

Article history:
Received 9 February 2016
Received in revised form
5 August 2016
Accepted 5 August 2016
Available online 7 August 2016

Keywords:
Forearc ophiolite
Mantle peridotites
Partial melting
Guleman
Turkey

ABSTRACT

The mantle section of Guleman ophiolite, southeast (SE) Turkey consists mainly of harzburgites and dunite lenses and large chromitite pods. The average Cr ratio = [100 × Cr/(Cr + Al) atomic ratio] of Cr-spinels in harzburgites and dunites is remarkably high (>63). The forsterite (Fo) content of olivine is between 90.9 and 92.3 in harzburgites and dunites. These features indicate that the harzburgites and dunites resulted from >35% of partial melting of a depleted mantle source. Discriminant geochemical diagrams based on the mineral chemistry of harzburgites indicate a supra-subduction zone (SSZ) origin. Orthopyroxene and clinopyroxene from the Guleman harzburgites have low CaO, Al_2O_3 and TiO_2 contents, resembling those of depleted harzburgites from modern forearcs and contrasting with moderately depleted abyssal peridotites. Consequently, we propose that the Guleman peridotites formed in a forearc setting during the subduction initiation that developed as a result of northward subduction of the southern branch of the Neo-Tethys in response to the convergence between the Arabian and Anatolian plates.

1. Introduction

Ophiolites represent fragments of ancient oceanic crust and upper mantle that were tectonically emplaced on land. A complete "Penrose" ophiolite includes tectonized peridotite, gabbro, sheeted dikes and pillow basalt (Anonymous, 1972). Ophiolites mark tectonic sutures, indicating both the location of ancient oceans and convergent plate boundaries, also known as collision zones (Dilek, 2003). Ophiolites form in a variety of tectonic settings including oceanic spreading center, backarc basins, forearc and arc. Ophiolites were classified as subduction-related and subduction-unrelated types by Dilek and Furnes (2014). The world's best-known ophiolites have petrological and geochemical characteristics that suggest formation above a subduction zone, an environment of formation known as a supra-subduction zone environment (Pearce et al., 1984). It is increasingly clear from the simple perspective of the plausible emplacement mechanism that forearcs are the most likely source of ophiolites (Casey and Dewey, 1984; Metcalf and Shervais, 2008; Milson, 2003). A relatively recent development in ophiolite studies has been the recognition of the importance of intra-oceanic subduction–initiation processes in ophiolite genesis (Stern and Bloomer, 1992; Stern et al., 2012). The subduction initiation rule (Whattam and Stern, 2011) predicts that ophiolites that form as a result of subduction initiation processes consist of a sequence of igneous rocks formed by a magma source that changed progressively in composition by the combined effects of melt depletion and subduction-related metasomatism.

The Guleman ophiolite is regarded as a fragment of Cretaceous oceanic lithosphere, composed of oceanic crust and upper mantle. The mantle sequence of the Guleman ophiolite is made up of harzburgite and dunite lenses and podiform chromitites. There have been a few studies on the mantle peridotites of the Guleman ophiolite (Özkan and Öztunalı, 1984; Bingöl, 1986). They suggest that the Guleman peridotite formed in a mid-oceanic ridge. In recent years, some researchers working on the SE Anatolian ophiolites accept that the SE Anatolian ophiolites are subduction-related ophiolites (Beyarslan and Bingöl, 2000, 2014; Bingöl et al., 2014; Karaoğlan et al., 2013).

The purpose of this study is to report the petrological data of the mantle peridotite with high Cr# spinel from the Guleman ophiolite. We then propose that the studied mantle peridotite genetically corresponds to subduction-related mantle and discuss that the Guleman ophiolite mantle rocks originated in the forearc setting.

* Corresponding author.
E-mail address: melahat.beyarslan@gmail.com (M. Beyarslan).

http://dx.doi.org/10.1016/j.jafrearsci.2016.08.013
1464-343X/

2. Geological setting

The Guleman ophiolite located 50 km southeast of Elazığ is one of the important ophiolitic massifs of the Southeast Anatolian Ophiolitic Belt. It consists of a core of mantle rocks overlain by an ultramafic sequence, layered and isotropic gabbro, and sheeted dykes. The ophiolite structurally overlies the Lower Miocene Lice Formation and is overlain by young sandstones and shales of the Upper Maashtrichtian–Lower Eocene Hazar Complex and Middle Eocene Maden Complex (Erdoğan, 1977; Özkaya, 1978; Perinçek, 1979; Perinçek and Çelikdemir, 1979; Righo de Righi and Cortesini, 1964) and tectonically overlain by Precambrian to Upper Triassic Bitlis metamorphic massif (Fig. 1A and B).

The mantle peridotites consist mainly of fresh and in-place serpentinized harzburgite tectonites with local bands and lenses of dunites with chromitite (Fig. 2A and B). Harzburgites are composed of olivine and orthopyroxene. They contain <2% clinopyroxene as exsolution lamellas in orthopyroxene. This suggests that the mantle peridotites are most depleted and, like forearc peridotites, they are the most depleted ultramafic rocks from any modern tectonic environment (Stern et al., 2012). They display high-temperature, low-pressure deformation (Bingöl, 1986). The dunites outcrop as small, dunitic lenses and thin envelopes around the chromite pods. They are intruded by pegmatitic, pyroxenite and gabbros and contain large amounts of podiform chromite deposits. The contact between the mantle peridotites and cumulate gabbros is represented by an ultramafic sequence.

There are numerous chromite occurences in Guleman ophiolite. Chromite occurences are present in ultramafic sequences (in the dunitic part) of the cumulate rocks, but the economically important deposits are mainly located in the mantle peridotites. Cassard et al. (1981) classified podiform chromitites into two types: concordant and discordant. In Guleman mantle peridotites, both types are present and additionally intermediate pod types also exist (Üşümezsoy, 1986). In the mantle peridotites the chromite pods are enveloped by dunite. The thickness of these envelopes may vary from a few centimeters to 3–4 m. The ultramafic sequence consists of dunites and chromian-rich layers. Along with dunites, the chromian-rich layers form the deepest cumulate layers and pass into dunite and wehrlite alternations higher in the sequences. This sequence is similar to the Kızılyüksek ultramafic cumulate of the Pozantı-Karsantı ophiolite (Bingöl, 1978). All rocks in the ultramafic cumulates possess adcumulate texture, and variable degrees of serpentinization are present in these rocks. Dunites contain disseminated and stratiform chromite layers at the centimeter to millimeter scale in the Kef area (Fig. 2B). Cumulus olivine (Fo 91–94%) constitutes 95% of the rock, serpentinized to variable degrees.

Gabbroic rocks above this transition zone display cumulate textures. The layering of the gabbro is defined by variation in the relative abundance of the main mineral phases (olivine, clinopyroxene, and plagioclase) or by the appearance or disappearance of one of these phases (Fig. 2C). Mineral-graded layers are common; size-graded layers are also observed. The thickness of the layers ranges from centimeters to decimeters. The layered gabbro transitions to isotropic gabbro towards the upper levels. Multiple and mutually intrusive relations between isotropic gabbro and a small body of leucocratic gabbro are common in the uppermost part of the plutonic sequence.

The main outcrop of the sheeted dyke complex occurs in the Northwest part of the Guleman ophiolite and is bounded on both sides by the gabbroic rocks (Fig. 2D). Isolated dykes cut through the cumulate and sheeted dykes. The volcanics associated with cumulates or sheeted dykes are missing, but there are some volcanic rocks (Caferi volcanics) that are tectonically separated from the

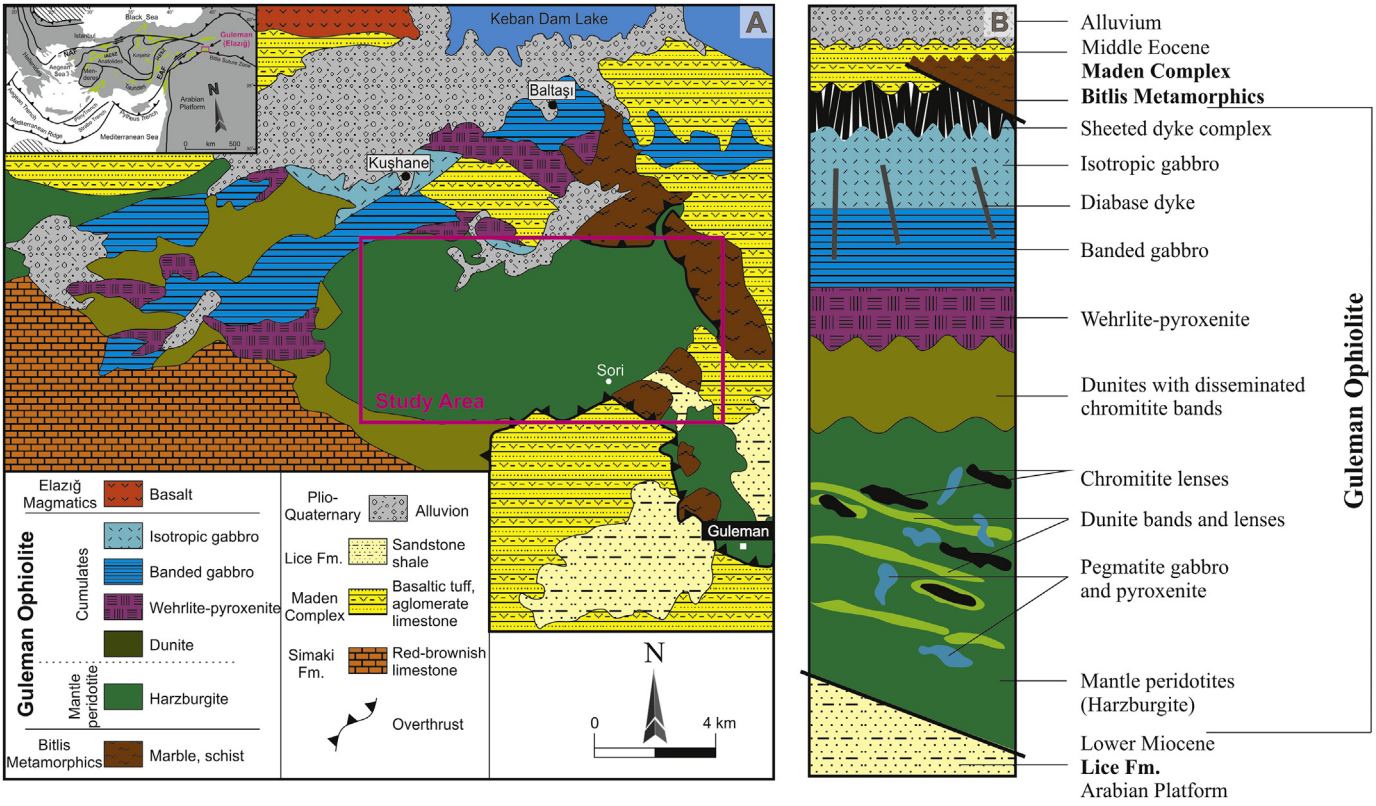

Fig. 1. (A) Geological map of Guleman area, (B) Tectono-stratigraphic columnar section of the Guleman ophiolite (modified from Beyarslan and Bingöl, 2014).

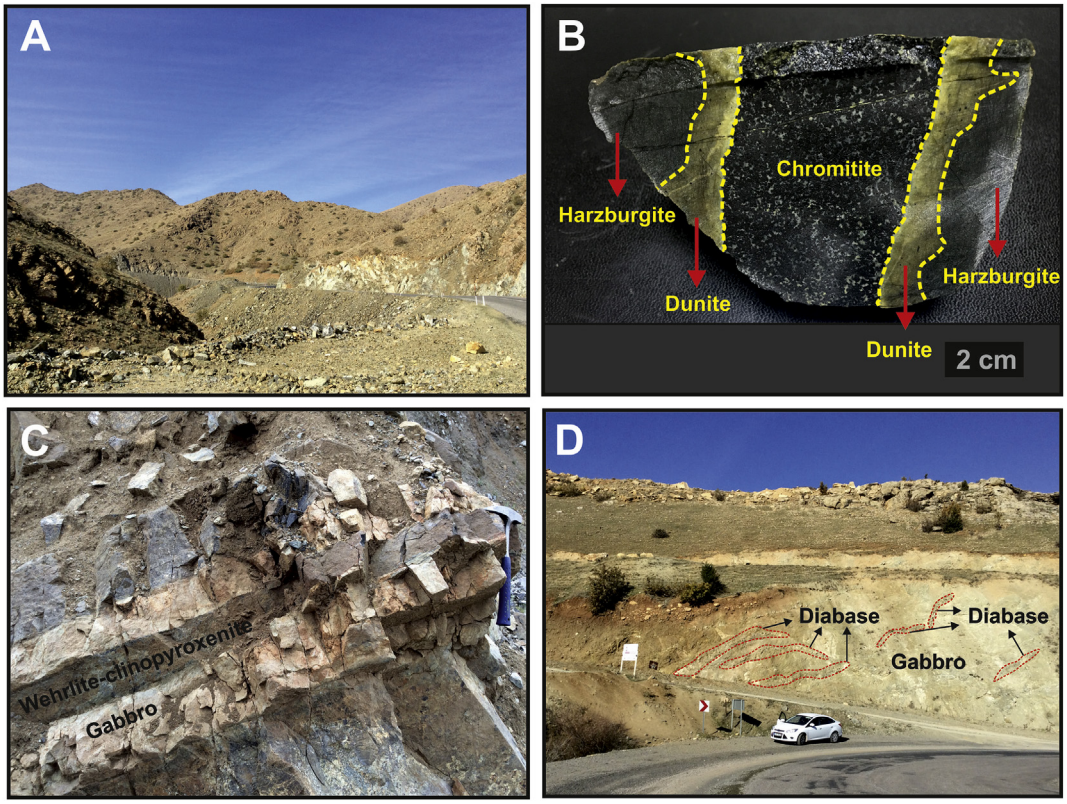

Fig. 2. Field photographs of Guleman ophiolite. (A) General view of mantle peridotites, on the Elazığ-Guleman way, near Soridağ (B) pyroxenite vein in harzburgite, Soridağ, (C) layered mafic cumulates, on the Elazığ-Guleman way (D) diabase dykes injected into cumulate gabbros on the Elazığ-Guleman way at the west of Baltaşı village.

main body and thrust over the Maden complex in the North. (Fig. 1). Caferi volcanics belong to the lower part of Upper Cretaceous Elazığ Igneous Complex, which constitute the upper volcanic unit of ophiolites (Beyarslan and Bingöl, 2014).

3. Petrography

The mantle peridotites of the Guleman ophiolite mainly consist of harzburgites (Fig. 3). They also contain small dunitic lenses and a thin envelope around the chromite pods. The dunites are serpentinized to variable degrees. Harzburgitic rocks are characterized by the near absence of primary clinopyroxene.

They commonly display high-temperature deformation fabrics such as kink-bands in olivines. The main texture of the harzburgites is porphyroclastic, indicating that the rocks are tectonites (Fig. 4A). Mylonitic textures can be seen occasionally. Orthopyroxene and spinel are stretched in some samples. Chrome-spinel exhibits vermicular and xenomorphic and, rarely, idiomorphic habits in peridotites. Clinopyroxene in harzburgites is rare. The harzburgites contain 70–80 modal % of olivine and 15–25 modal % of orthopyroxene. The minor phases are clinopyroxene (2–3 modal %) and chrome-spinel (2–3 modal %). The peridotites show some extent of serpentinization. A mesh texture is formed due to alteration of olivine forming chrysotile and lizardite (Fig. 4B). Porphyroclastic orthopyroxene displays plastic deformational features such as undulatory extinction, strain lamella, kink bands, rotation, and lobate boundaries. Most likely, plastic deformation occurred when the rocks were very close to the solidus temperature (Boudier et al., 1982).

4. Analytical method

Following the observation of 50 thin sections prepared from the mantle peridotites, 18 samples (16 harzburgites, 2 dunites) were chosen for whole-rock chemical analysis using an Inductively Coupled Plasma Mass Spectroscopy (ICP-MS) (Groups 4A and 4B) instrument from ACME Analytical Laboratory at Vancouver (Canada). The total abundances of major oxides and several minor elements were determined on 0.2 g aliquot for each of the samples following a $LiBO_2$ fusion dilute nitric digestion. Major oxides have a detection limit of 0.01% except for SiO_2 with 0.1%. Major and some detectable trace elements of the analyzed samples are listed in Table 1. Major element analysis of minerals of mantle peridotites

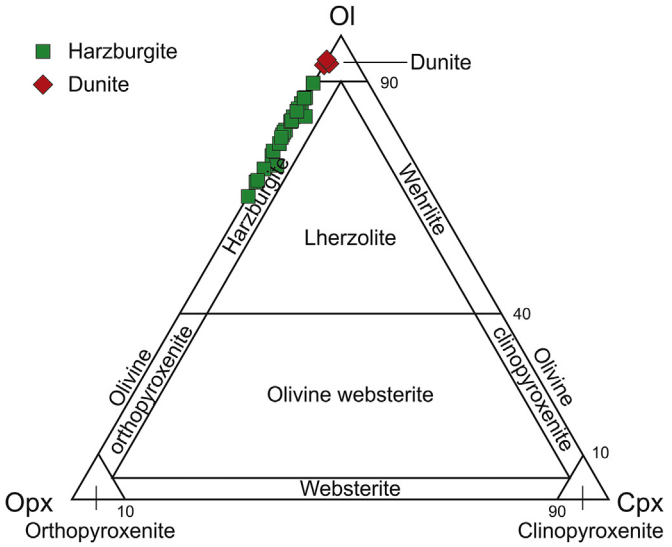

Fig. 3. Modal plot of the studied samples in olivine-orthopyroxene-clinopyroxene diagram.

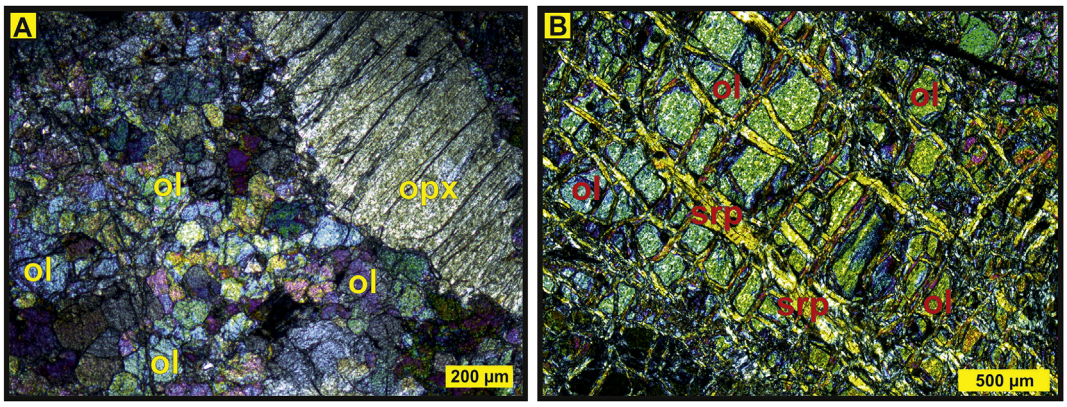

Fig. 4. (A) Crashed olivine crystals, porphiroclastic texture (Crossed polars: CP) (ol: olivine, opx: orthopyroxene), (B) mesh texture in serpantinized olivine minerals (CP) (ol: olivine, srp: serpentine).

Table 1
Whole rock major oxides (wt%) and some trace elements abundances (ppm) in peridotite samples of Guleman ophiolite. LOI: Loss on ignition; Serp% = (100/18)*LOI (wt%); DL: Detection limits.

Sample rock type	MG1	MG2	MG7	MG8	MG10	MG11	MG12	MG20	MG24	MG26	MG27	MG28	MG29	MG33	MG35	MG36	MG37	MG38	DL
	Hrz.	Dun.	Hrz.	Hrz.	Hrz.	Hrz.	Hrz.	Hrz.	Dun.	Hrz.	Hrz.	Hrz.	Hrz.	Hrz.	Hrz.	Hrz.	Hrz.	Hrz.	
SiO_2	43.89	43.29	42.46	43.21	43.57	41.53	42.22	43.09	40.24	43.84	43.42	42.75	43.31	43.35	44.46	42.21	43.82	43.67	0.01
TiO_2	<0.01	<0.01	<0.01	<0.01	<0.01	<0.01	0.04	<0.01	<0.01	<0.01	<0.01	<0.01	<0.01	<0.01	<0.01	<0.01	<0.01	<0.01	0.01
Al_2O_3	0.33	0.30	0.33	0.36	0.20	0.24	2.23	0.36	0.34	0.34	0.36	0.53	0.16	0.41	0.46	0.35	0.33	0.19	0.01
Fe_2O_3	9.12	9.10	8.60	8.76	9.03	8.56	7.91	8.86	8.08	8.26	8.56	8.96	8.66	8.72	8.22	8.62	8.86	8.80	0.04
MnO	0.13	0.13	0.12	0.12	0.13	0.12	0.12	0.12	0.11	0.12	0.12	0.12	0.12	0.12	0.12	0.12	0.12	0.12	0.01
MgO	43.69	44.98	44.09	44.72	44.92	43.83	34.72	42.70	43.86	44.31	44.09	43.65	43.60	43.63	43.97	43.64	44.04	44.00	0.01
CaO	0.53	0.49	0.47	0.44	0.41	0.33	2.30	0.55	0.30	0.38	0.46	0.65	0.27	0.49	0.34	0.34	0.39	0.32	0.01
Na_2O	<0.01	<0.01	<0.01	<0.01	<0.01	<0.01	0.05	0.04	<0.01	0.02	0.01	<0.01	<0.01	<0.01	<0.01	<0.01	<0.01	<0.01	0.01
K_2O	<0.01	<0.01	<0.01	<0.01	<0.01	<0 + A1G13	<0.01	<0.01	<0.01	<0.01	<0.01	<0.01	<0.01	<0.01	<0.01	<0.01	<0.01	<0.01	0.01
LOI	1.60	1.00	3.20	1.70	1.10	4.80	9.70	3.60	6.40	1.90	2.30	2.60	2.60	1.90	1.00	3.30	1.00	1.50	
Σ	99.95	99.95	99.95	99.95	99.97	99.95	99.95	99.95	99.96	99.94	99.94	99.95	99.29	99.28	99.28	99.28	99.28	99.28	
%Serp.	8.9	5.6	17.8	9.4	6.1	26.7	53.9	20.0	35.6	10.6	12.8	14.4	14.4	10.6	5.6	18.3	5.6	8.3	
Ni	2521	2568	2509	2554	2595	2464	2105	2441	2566	2480	2546	2443	2324	2227	2271	2269	2370	2253	20.0
Sc	9	9	8	8	9	7	13	9	6	7	9	9	7	8	6	7	8	8	1.0
Co	109.6	112.7	101.8	102.1	111.7	103.6	91.6	100.8	104.9	116.9	109.7	114.0	106.7	110.2	114.2	112.5	114.7	111.1	0.2
Ga	0.8	1.1	0.6	0.9	0.6	0.7	2.2	0.8	0.6	1.6	1.0	<0.5	0.5	1.2	1.0	0.6	0.9	<0.5	0.5
V	31	30	28	27	21	25	58	34	21	35	27	38	21	31	24	29	27	26	8.0
Zr	1.4	0.3	6.9	0.6	1.2	0.4	0.7	1.8	1.6	0.6	1.6	2.3	0.1	0.2	0.2	0.2	0.3	0.3	0.1
Cu	9.6	13.4	5.5	2.8	5.7	3.3	24.2	3.6	2.1	3.1	38.0	10.8	2.2	4.5	2.4	2.5	4.2	4.0	0.1
Zn	25	27	25	25	27	28	24	22	24	24	25	25	28	26	24	26	26	25	1.0

Table 2
Average composition (wt%) and standard deviation (σ) for analyses of spinel in each sample. n: number of spot analyses performed; Mg# = 100 × Mg/(Mg + $Fe2^+$); Cr# = 100 × Cr/(Cr + Al); $Fe2^+$# = 100 × $Fe2^+$/(Mg + $Fe2^+$); –: below detection limits.

Sample rock type n	MG 10		MG 11		MG 20		MG 26		MG 27		MG 29		MG 32		MG 36	
	Hrz.		Hrz.		Hrz.		Hrz.		Hrz.		Hrz.		Hrz.		Hrz.	
	27	σ	19	σ	22	σ	25	σ	22	σ	26	σ	18	σ	20	σ
SiO_2 SiO_2	0.02	0.02	0.02	0.02	0.02	0.02	0.02	0.02	0.01	0.01	0.02	0.03	0.02	0.02	0.01	0.02
TiO_2 TiO_2	0.02	0.02	0.05	0.02	0.02	0.02	0.03	0.02	0.03	0.02	0.03	0.03	0.03	0.02	0.06	0.03
Al_2O_3 Al_2O_3	12.02	0.93	15.07	0.61	15.61	0.73	15.40	1.55	17.32	1.09	10.04	0.41	19.67	0.90	18.68	1.49
Cr_2O_3 Cr_2O_3	56.58	1.25	53.20	1.04	50.79	1.11	53.08	1.98	49.75	1.39	58.44	0.81	49.21	1.19	48.56	1.66
FeO	20.53	0.52	19.57	0.49	23.64	0.64	18.97	0.33	21.10	0.41	21.70	0.74	18.37	0.48	20.56	0.72
MnO	0.90	0.23	0.62	0.22	0.89	0.25	0.86	0.18	0.85	0.17	0.95	0.17	0.81	0.20	0.77	0.13
MgO	9.51	0.34	10.55	0.36	8.23	0.26	11.03	0.22	10.83	0.27	8.81	0.33	11.77	0.27	11.30	0.51
NiO	–	–	–	–	–	–	–	–	–	–	–	–	–	–	–	–
CaO	0.01	0.02	0.01	0.01	0.01	0.01	0.01	0.02	0.01	0.01	0.01	0.01	0.01	0.02	0.01	0.01
Na_2O Na_2O	–	–	–	–	–	–	–	–	–	–	–	–	–	–	–	–
K_2O K_2O	–	–	–	–	–	–	–	–	–	–	–	–	–	–	–	–
$P_2O_5P_2O_5$	–	–	–	–	–	–	–	–	–	–	–	–	–	–	–	–
ZnO	0.14	0.10	0.18	0.08	0.31	0.12	0.16	0.10	0.16	0.09	0.16	0.11	0.16	0.10	0.14	0.08
Σ	99.73		99.27		99.51		99.57		100.05		100.16		100.03		100.09	
Mg#	45.20	1.47	48.99	1.39	38.30	1.29	50.88	0.76	47.77	1.05	41.97	1.68	53.30	1.06	49.46	1.94
Cr#	75.95	1.75	70.30	1.08	68.57	1.40	69.82	2.82	65.84	2.01	79.61	0.84	62.66	1.62	63.56	2.54
Fe^{+2}#	54.80	1.47	51.01	1.39	61.70	1.29	49.12	0.76	52.23	1.05	58.03	1.68	46.70	1.06	50.54	1.94

Table 3
Average composition (wt%) and standard deviation (σ) for analyses of clinopyroxene in each sample. n: number of spot analyses performed; Mg# = 100 × Mg/(Mg + $Fe2^+$); Cr# = 100 × Cr/(Cr + Al); –: below detection limits.

Sample rock type n	MG 10		MG 11		MG 26		MG 27		MG 29		MG 32		MG 36	
	Hrz.		Hrz.		Hrz.		Hrz.		Hrz.		Hrz.		Hrz.	
	23	σ	16	σ	17	σ	23	σ	11	σ	20	σ	21	σ
SiO_2	54.32	0.43	53.78	0.50	54.04	0.56	53.97	0.47	54.55	0.47	53.97	0.36	54.08	0.31
TiO_2	0.01	0.02	0.01	0.01	0.01	0.01	0.02	0.02	0.02	0.02	0.01	0.02	0.03	0.02
Al_2O_3	0.69	0.11		0.16	0.85	0.15	1.13	0.21	0.52	0.10	1.23	0.27	1.21	0.13
Cr_2O_3	0.37	0.08	0.43	0.11	0.42	0.09	0.52	0.14	0.37	0.07	0.54	0.15	0.47	0.10
FeO	1.81	0.15	1.72	0.16	1.72	0.15	1.76	0.19	1.78	0.13	1.67	0.12	1.81	0.17
MnO	0.08	0.03	0.07	0.03	0.05	0.03	0.06	0.04	0.06	0.04	0.07	0.03	0.06	0.02
MgO	18.18	0.42	18.27	0.27	18.35	0.32	18.03	0.23	18.26	0.27	17.99	0.21	18.23	0.53
NiO	–	–	–	–	–	–	–	–	–	–	–	–	–	–
CaO	23.70	0.63	24.08	0.45	23.96	0.40	24.37	0.37	24.20	0.47	24.49	0.33	24.27	0.85
Na_2O	0.03	0.02	0.03	0.02	0.08	0.02	0.03	0.02	0.13	0.03	0.02	0.02	0.04	0.02
K_2O	0.00	0.00	0.00	0.00	0.01	0.01	0.00	0.01	0.01	0.01	0.01	0.01	0.01	0.01
Σ	99.20		99.27		99.49		99.89		99.90		99.99		100.20	
Mg#	94.71	0.36	94.99	0.42	95.00	0.38	94.80	0.54	94.82	0.32	95.05	0.34	94.73	0.41
Cr#	26.59	2.21	24.55	2.87	25.01	2.19	23.39	3.41	32.53	2.80	22.47	1.94	20.53	2.34

Table 4
Average composition (wt%) and standard deviation (σ) for analyses of orthopyroxene in each sample. n: number of spot analyses performed; Mg# = 100 × Mg/(Mg + $Fe2^+$); Cr# = 100 × Cr/(Cr + Al); Wo = 100 × Ca/(Ca + Mg + $Fe2^+$); En = 100 × Mg/(Ca + Mg + $Fe2^+$); Fs = 100 × $Fe2^+$/(Ca + Mg + $Fe2^+$); –: below detection limits.

Sample rock type n	Mg 10		Mg 11		Mg 20		Mg 26		Mg 27		Mg 29		Mg 32		Mg 36	
	Hrz.		Hrz.		Hrz.		Hrz.		Hrz.		Hrz.		Hrz.		Hrz.	
	23	σ	13	σ	10	σ	21	σ	21	σ	10	σ	20	σ	10	σ
SiO_2	57.18	0.36	57.07	0.42	56.83	0.22	57.26	0.53	57.22	0.43	57.79	0.52	57.18	0.67	56.76	0.51
TiO_2	0.01	0.02	0.02	0.02	0.01	0.01	0.01	0.02	0.02	0.02	0.01	0.02	0.02	0.01	0.02	0.02
Al_2O_3	0.66	0.08	0.99	0.06	1.14	0.08	0.94	0.09	1.19	0.11	0.51	0.04	1.34	0.13	1.25	0.17
Cr_2O_3	0.28	0.07	0.40	0.05	0.45	0.04	0.38	0.10	0.39	0.10	0.21	0.06	0.47	0.08	0.34	0.10
FeO	5.33	0.12	5.15	0.15	5.44	0.23	4.99	0.15	5.33	0.14	5.36	0.12	5.32	0.20	5.36	0.14
MnO	0.14	0.04	0.12	0.02	0.13	0.02	0.12	0.03	0.13	0.03	0.13	0.03	0.12	0.04	0.12	0.04
MgO	34.86	0.31	34.75	0.33	34.24	0.40	34.89	0.34	34.83	0.28	35.49	0.34	34.86	0.48	35.18	0.28
NiO	–	–	–	–	–	–	–	–	–	–	–	–	–	–	–	–
CaO	0.72	0.25	0.98	0.43	1.04	0.34	0.78	0.24	0.75	0.22	0.71	0.21	0.87	0.54	0.64	0.22
Na_2O	0.01	0.01	0.00	0.01	0.01	0.01	0.00	0.01	0.01	0.01	0.01	0.01	0.01	0.01	0.01	0.01
K_2O	0.00	0.01	0.00	0.01	0.01	0.01	0.00	0.01	0.00	0.00	0.01	0.01	0.00	0.01	0.00	0.00
Σ	99.20		99.50		99.29		99.39		99.86		100.23		100.17		99.69	
Mg#	92.1	0.2	92.3	0.2	91.8	0.3	92.6	0.2	92.1	0.2	92.2	0.1	92.1	0.2	92.1	0.2
Cr#	22.3	4.4	21.4	1.9	21.0	2.1	21.2	5.1	17.6	3.0	21.4	3.9	18.9	2.3	15.2	3.1
Wo	1.3	0.5	1.8	0.8	2.0	0.7	1.5	0.4	1.4	0.4	1.3	0.4	1.6	1.0	1.2	0.4
En	90.9	0.5	90.6	0.7	90.0	0.6	91.2	0.4	90.8	0.4	91.0	0.3	90.6	0.9	91.0	0.5
Fs	7.8	0.2	7.5	0.2	8.0	0.3	7.3	0.2	7.8	0.2	7.7	0.2	7.8	0.3	7.8	0.2

Table 5
Average composition (wt%) and standard deviation (σ) for analyses of olivine in each sample. n: number of spot analyses performed; Fo = 100 × Mg/(Mg + $Fe2^+$); –: below detection limits.

Sample rock type n	Mg 10		Mg 11		Mg 12		Mg 20		Mg 26		Mg 27		Mg 29		Mg 32		Mg 36	
	Hrz.		Hrz.		Hrz.		Hrz.		Hrz.		Hrz.		Hrz.		Hrz.		Hrz.	
	27	σ	21	σ	7	σ	27	σ	16	σ	22	σ	16	σ	21	σ	27	σ
SiO_2	40.26	0.26	40.41	0.24	39.91	0.26	40.31	0.31	40.48	0.25	40.39	0.40	40.51	0.26	40.34	0.23	40.35	0.35
TiO_2	0.01	0.02	0.01	0.01	0.01	0.01	0.01	0.02	0.01	0.01	0.01	0.01	0.01	0.01	0.02	0.02	0.01	0.01
Al_2O_3	0.00	0.01	0.00	0.01	0.01	0.02	0.01	0.01	0.00	0.01	0.01	0.01	0.01	0.01	0.01	0.01	0.01	0.04
Cr_2O_3	0.05	0.14	0.01	0.01	0.01	0.01	0.01	0.02	0.00	0.00	0.01	0.02	0.00	0.01	0.01	0.01	0.02	0.05
FeO	7.92	0.49	7.88	0.27	8.89	0.08	8.30	0.41	7.52	0.13	7.83	0.28	7.90	0.18	8.04	0.16	7.90	0.26
MnO	0.10	0.03	0.10	0.03	0.13	0.03	0.11	0.03	0.09	0.03	0.09	0.04	0.10	0.03	0.10	0.03	0.10	0.03
MgO	50.48	0.38	50.59	0.44	49.69	0.35	50.06	0.47	50.97	0.23	50.70	0.34	50.77	0.28	50.90	0.23	50.77	0.45
NiO	0.40	0.05	0.38	0.05	0.39	0.04	0.40	0.07	0.41	0.05	0.40	0.04	0.37	0.06	0.38	0.05	0.40	0.03
CaO	0.01	0.02	0.02	0.02	0.01	0.01	0.01	0.01	0.01	0.01	0.01	0.01	0.01	0.01	0.01	0.01	0.02	0.01
Na_2O	–	–	–	–	–	–	–	–	–	–	–	–	–	–	–	–	–	–
K_2O	–	–	–	–	–	–	–	–	–	–	–	–	–	–	–	–	–	–
Σ	99.24		99.39		99.04		99.22		99.50		99.45		99.69		99.81		99.53	
Fo	91.90	0.01	91.96	0.00	90.88	0.00	91.48	0.00	92.35	0.00	92.02	0.00	91.97	0.00	91.85	0.00	91.97	0.00

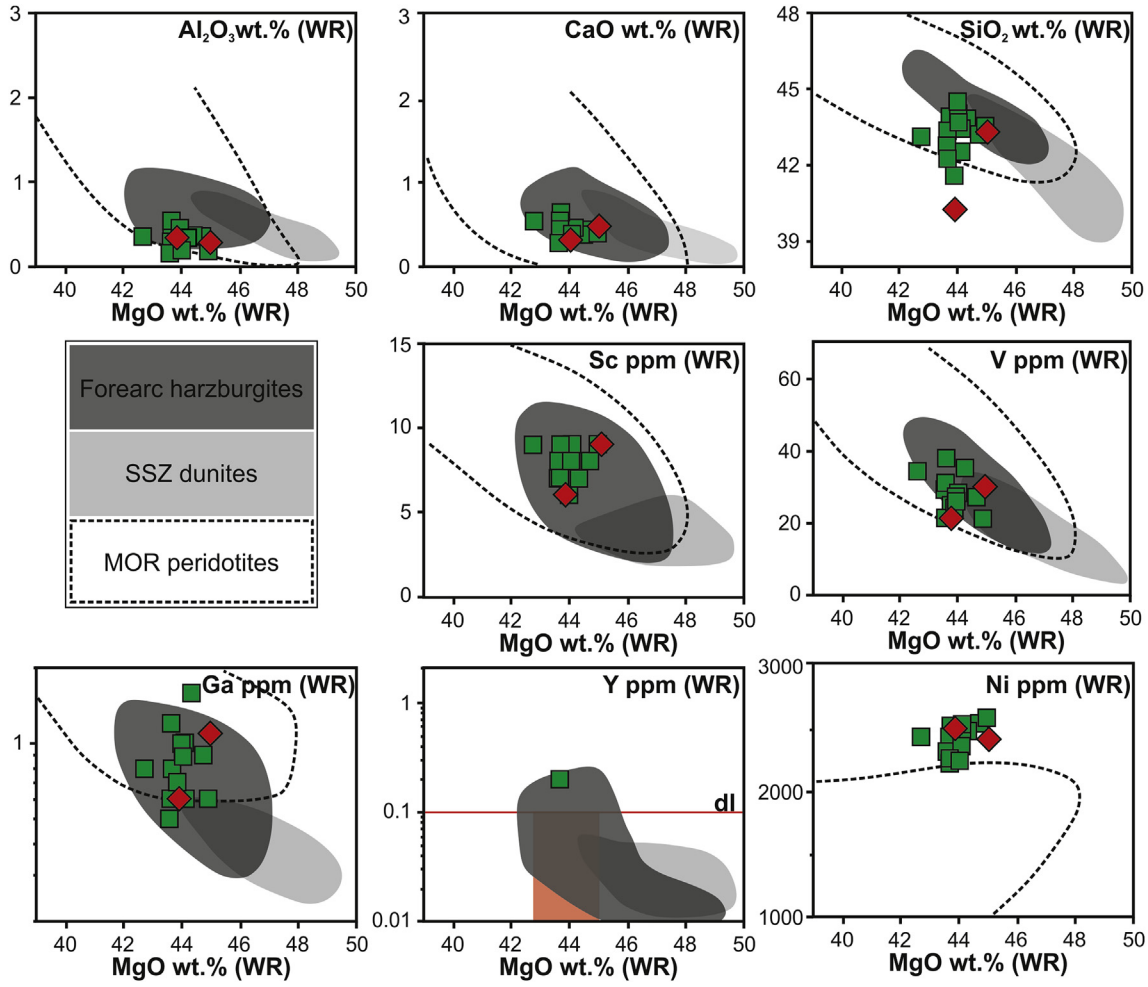

Fig. 5. MgO wt% versus Al_2O_3, CaO, SiO_2 wt%, Sc, V, Ga and Ni diagram (MOR peridotites from Niu (2004), forearc harzburgite and SSZ dunite from Parkinson and Pearce (1998)).

was carried out with a wavelength dispersive microprobe JXA 8900R (JEOL) at the Institute of Earth Sciences, Academia Sinica, Taipei, Taiwan. The accelerating voltage and beam current were 15 kV and 12 nA respectively. The Fe^{3+} and Fe^{2+} contents of the minerals were calculated based on stoichiometric criteria. The detailed analytical procedure and precision were reported by Shellnutt and Iizuka (2013). Analytical results are given in Tables 2–5.

4.1. Whole-rock geochemistry

The low Al_2O_3 (0.44 wt% on average) and CaO (0.40 wt% on average) contents testify their highly depleted nature.

The rare-earth element (REE) contents are very low (commonly below the detection limits). Hence, the REEs were not used in this study. The trace elements are also depleted in the studied samples, many of which are below the detection limits, except elements such as Ni, Sc, Co, Ga, and V, which are enriched in all samples. MgO versus other oxides and Sc, V, Ga, Y, and Ni ppm discrimination diagrams are used to distinguish the domains among forearc harzburgites, SSZ dunites and MOR peridotites. These criteria show that all harzburgites of the Guleman ophiolite plot within the forearc harzburgites field (Fig. 5). In the CaO wt% versus Al_2O_3 wt% diagram also, all harzburgites and dunites plot in the forearc peridotite field (Fig. 6).

4.2. Mineral chemistry

4.2.1. Spinel

The harzburgite contains high-Cr with Cr# in the range of 66–80%. The Cr_2O_3 content of spinel in harzburgites is high with an average of 52.45 wt%. The Al_2O_3 content displays narrow ranges (10.04–19, 64 wt%). Spinels in harzburgites are chromian spinels (the amount of TiO_2 is 0.02–0.03 wt%) (Table 2).

TiO_2 versus Al_2O_3 of spinel is used to distinguish between supra-subduction zone ophiolites and MOR ophiolites (Kamenetsky et al., 2001). This criterion shows that the peridotites of the Guleman ophiolites are SSZ peridotites (Fig. 7). Mg# [$=100 \times Mg/(Mg + Fe^{2+})$] versus Cr# in spinels is used to determine the tectonic environment. The spinels plot in the forearc peridotites field (Fig. 8). In the relationships between Cr# of spinel and Fo content of olivines, the harzburgites plot within the olivine-spinel-mantle array (OSMA) field in the diagram of Arai (1987; 1994a, 1994b) indicating residual mantle peridotites. The Cr# of spinel is a good indicator of the degree of partial melting for mantle-derived spinel peridotite (Arai, 1994b; Dick and Bullen, 1984). When the harzburgites are plotted within the Arai diagram Arai (1994a), it can be seen that the degree of partial melting is between 35% and 45% (Fig. 8). The Cr# versus TiO_2 plot of spinels is used to distinguish between forearc and abyssal peridotite. The Guleman peridotites plot within the forearc peridotite field (Fig. 9).

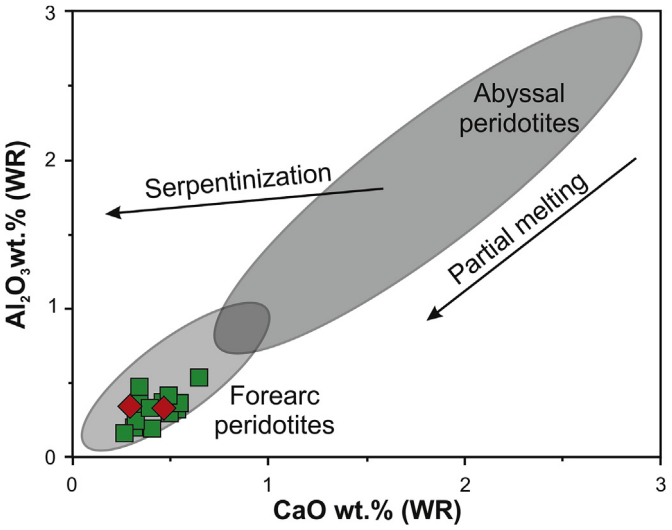

Fig. 6. Variation diagram of Guleman peridotite in CaO wt% versus Al_2O_3 diagram (Pearce et al., 1992).

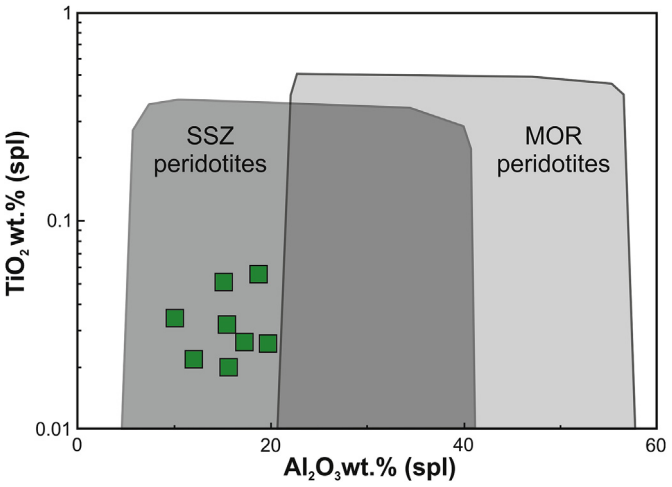

Fig. 7. Al_2O_3 wt% (in spinel) versus TiO_2 wt% (in spinel) diagram (Kamenetsky et al., 2001).

4.2.2. Clinopyroxene

Clinopyroxene in harzburgites occurs as exsolution lamellas in orthopyroxenes. Clinopyroxenes in the harzburgite are characterized by 0.37–0.54 wt% Cr_2O_3 and 0.01–0.03 TiO_2 (Table 3). Using the plot of Al_2O_3 in clinopyroxene versus the other oxides in clinopyroxene; the harzburgites fall within the forearc peridotite field (Fig. 10).

4.2.3. Orthopyroxene

The chemical composition of orthopyroxene in harzburgites is enstatite with Mg# of 91.8–92.6%, 0.21–0.47% Cr_2O_3 and low TiO_2 (<0.02 wt%) (Table 4).

4.2.4. Olivine

The chemical composition of olivine is close pure forsterite, and Mg# is 90.88–92.35%. The NiO content is 0.37–0.41 wt% (Table 5). In the Fo (olivine) versus NiO wt% diagram, the studied olivine is plotted in the forearc peridotites (Fig. 11).

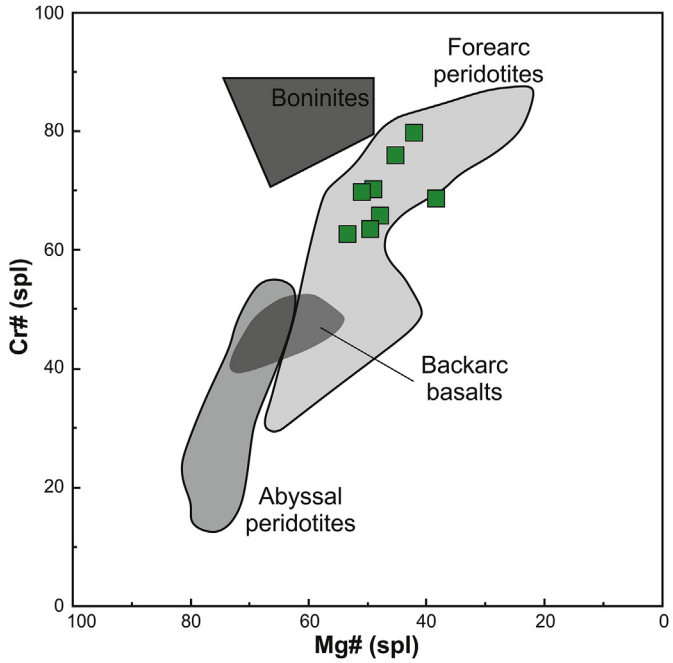

Fig. 8. Composition of spinels in Guleman peridotites, plotted on Mg# [=100 × Mg/(Mg + Fe^{2+}) atomic ratio] versus Cr# [=100 × Cr/(Cr + Al) atomic ratio] diagram. Abyssal peridotite and boninite field from Dick and Bullen (1984), forearc peridotite field from Ishii et al. (1992); backarc basin basalts field from Allan (1994).

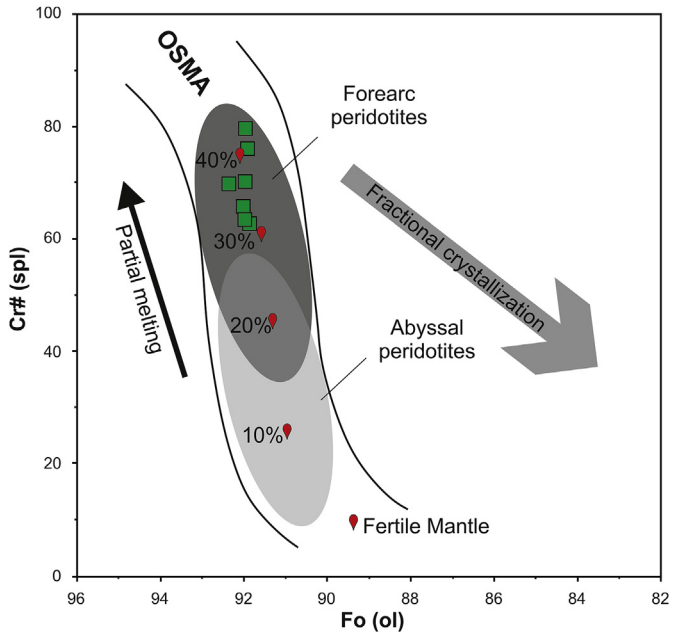

Fig. 9. Compositional relationship between Fo content of olivine and Cr# of spinel and degree of partial melting in the harzburgite and dunite from the Guleman ophiolite. OSMA: olivine-spinel mantle array; Arai, 1994a).

5. Discussion and conclusion

Mantle peridotites of the Guleman ophiolite composed of harzburgites and dunite lenses with chromitite are interpreted to be restites that experienced high degrees of partial melting beyond the stability of clinopyroxene and therefore represent refractory mantle (see Fig. 12). Earth has had mantle since shortly after it

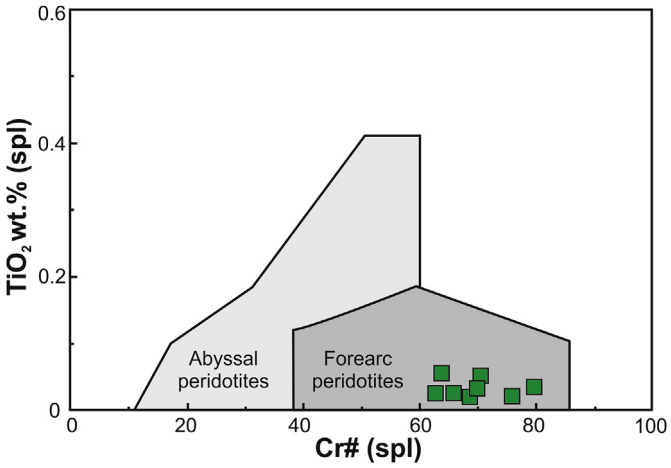

Fig. 10. Relationship between Cr# and TiO_2 wt% of spinels in studied harzburgites (the abyssal peridotites field from Dick and Bullen, 1984; Arai, 1994a; the forearc peridotite field from Bloomer and Hawkins, 1983; Bloomer and Fisher, 1987; Ishii et al., 1992; Parkinson and Pearce, 1998).

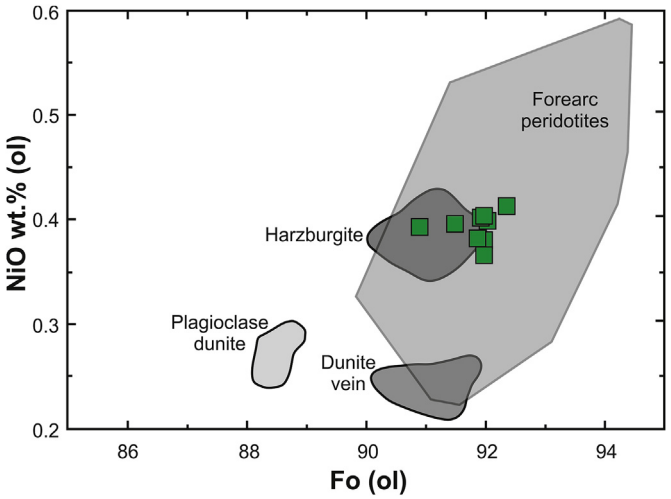

Fig. 12. Relationship between Fo of olivine contents and NiO wt% in olivine of Guleman peridotite. Forearc peridotites field from Ishii et al. (1992) various areas for mantle peridotites from Constantin et al. (1995).

formed, but it has been modified by melt extraction and mixing with subducted materials. Idealized compositions are useful for this discussion. For example, "primitive" mantle (PM) refers to an idealized chemical composition after the core segregated but before the continental crust was extracted (Stern et al., 2012). Several studies have estimated PM compositions, including high (89–90%) Mg# [$=100 \times Mg/(Mg + Fe^{2+})$], 2.8–3.7 wt% CaO and 3.5–4.5 wt% Al_2O_3 (Lyubetskaya and Korenaga, 2007). Primitive Mantle (PM) is known as lherzolite. Partial melting of PM diminishes the abundance of clinopyroxene, CaO and Al_2O_3 and increases Cr# in the residual spinel. Peridotite compositions are sensitive indicators of tectonic setting (e.g., Bonatti and Michael, 1989). Some major oxides such as Al_2O_3 and CaO are especially useful for evaluating the degree of partial melting and peridotite depletion (Ishii et al., 1992; Pearce et al., 1992). Clinopyroxene contains nearly all CaO in peridotite, whereas spinel contains nearly 35% Al_2O_3. Melt depletion reduces the proportion of clinopyroxene, so the residue progressively changes from lherzolite to harzburgite, and extreme melt depletion yields dunite (Stern et al., 2012). Modal mineralogy and primary mineral compositions of the upper mantle peridotites are considered as a key to constrain the extent of partial melting, fluid phase enrichment, and mantle–melt interaction processes subsequent to melt extraction (Bonatti and Michael, 1989; Choi et al., 2008; Hellebrand et al., 2001; Morishita et al.,

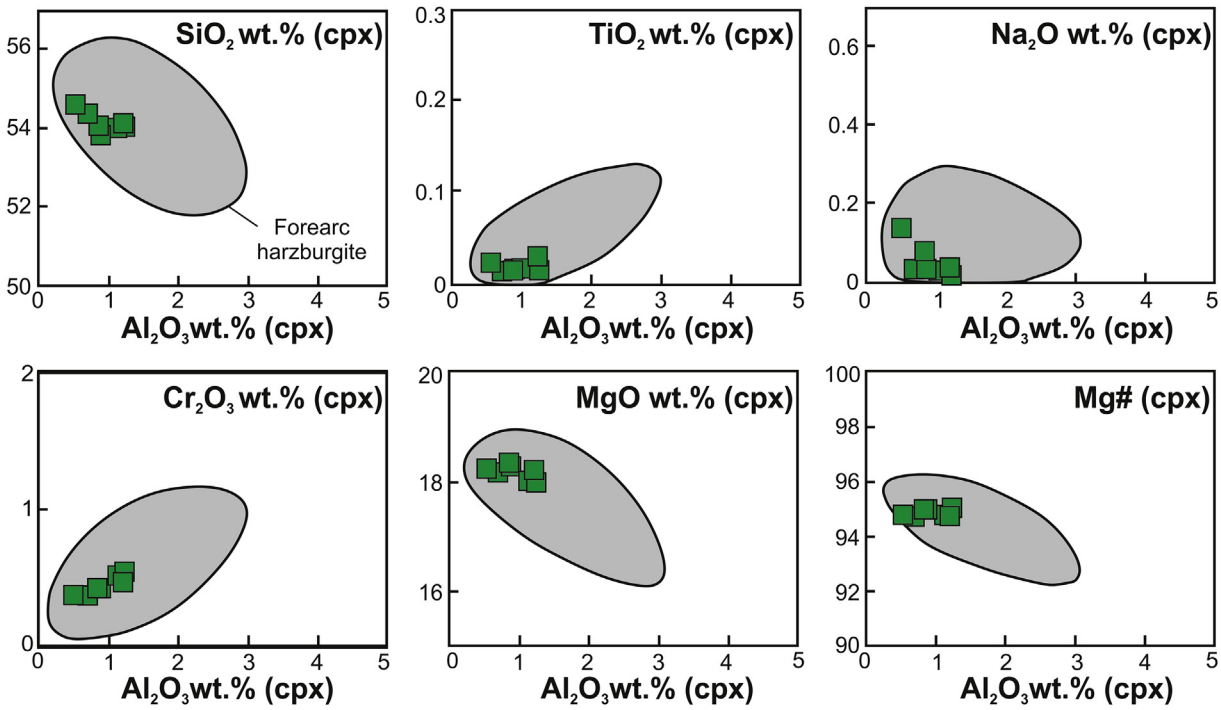

Fig. 11. Relationship between Al_2O_3 wt% and other oxides wt% in clinopyroxenes from Guleman peridotites. Forearc peridotite field from Parkinson and Pearce (1998) and Pearce et al. (2000).

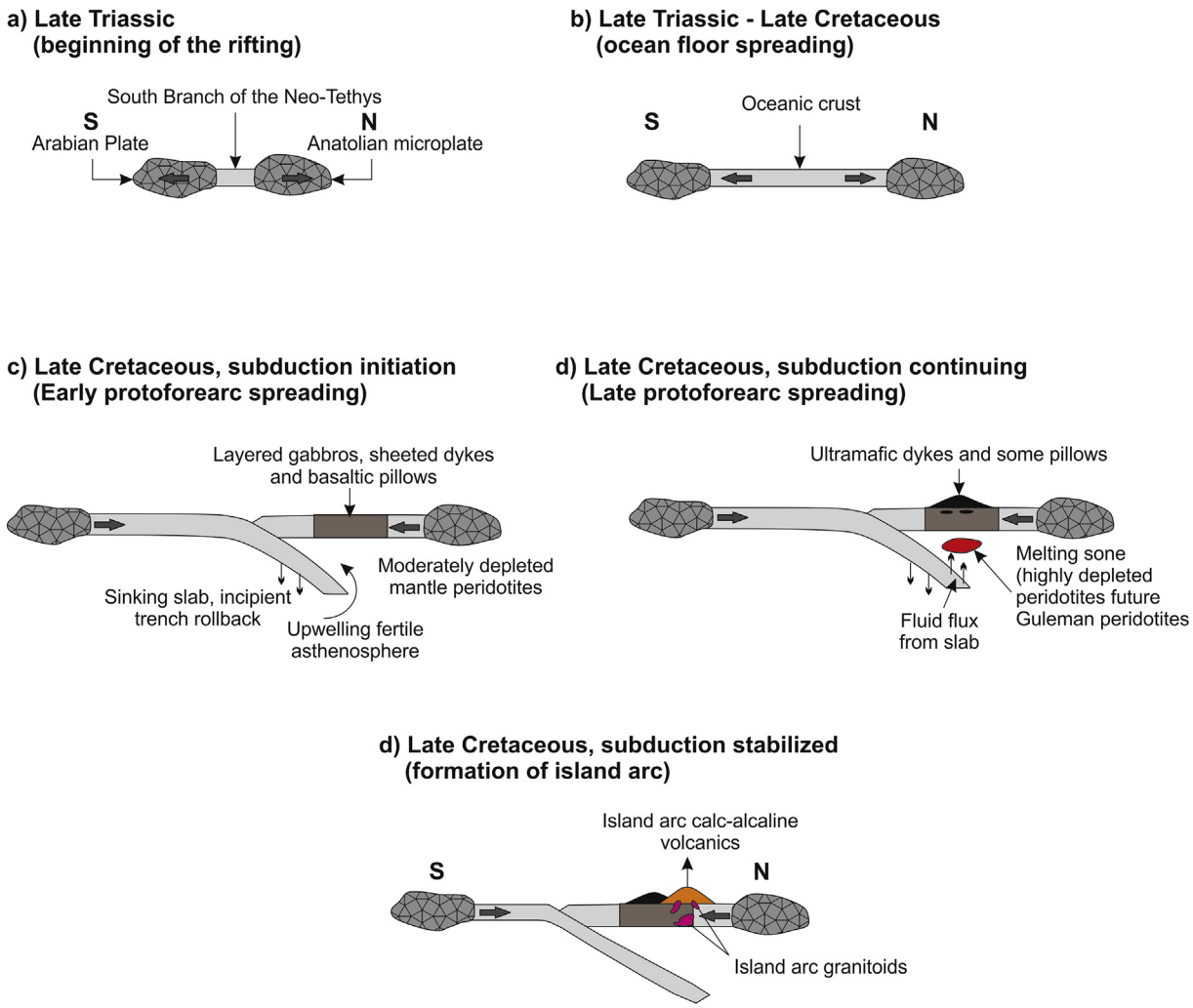

Fig. 13. Schematic model for the formation and evolution of the Southeast Anatolian ophiolites.

2011; Seyler et al., 2007). Pyroxenes in the SSZ peridotites, which experienced higher degrees of partial melting, are depleted in the moderately incompatible elements such as Al, Ti, and Na. Olivine in these peridotites also has higher Fo contents. These characteristic features are commonly found in minerals in equilibrium with boninitic melt (Zhou et al., 1996; Melcher et al., 1997). The Al_2O_3 content in pyroxenes and Cr-spinels of mantle peridotites are sensitive to the degree of mantle melting, decreasing systematically with increasing peridotite depletion.

The low Al_2O_3 (0.44 wt% on average) and CaO (0.40 wt% on average) contents of harzburgite and dunite of the Guleman peridotite indicates their highly depleted nature, which is confirmed by low clinopyroxene content. The harzburgites and dunites are characterized by the high Cr# (>62.66%) of spinel and Fo of olivine (90.9–92.3%). The harzburgites and dunites fall within the OSMA field of the diagram of Arai (1987; 1994a, 1994b), indicating their residual mantle peridotite composition. The Cr# of spinel is a good indicator for the degree of partial melting of the mantle-derived spinel peridotite (Dick and Bullen, 1984; Arai, 1994a). The Cr# value is also useful in discriminating the tectonic setting of peridotites. All Cr# values of the spinels in the Guleman peridotites indicate a high degree of partial melting (>30%) and a forearc tectonic setting environment. The diagrams, which are useful to discriminate the tectonic settings, indicate that the Guleman peridotites were formed in a forearc setting (Figs. 4–11). The unusually depleted nature of forearc peridotites requires unusual melting conditions: abnormally high temperature, volatile flux, or both. Highly depleted harzburgites, dunites and chromitites in the ophiolites form by second-stage melts of the mantle wedge overlying the new subduction zone. These melts form in response to continued melting of previously depleted asthenosphere brought about by increasing flux of fluids and melts from the subducting slab (Shervais, 2000). According to Whattam and Stern (2011), most ophiolites are fragments of exhumed forearcs, and forearcs formed during subduction initiation allowing us to use ophiolites to explore how subduction zones form. The Guleman mantle peridotites contain many podiform chromite deposits with high Cr# chromites (Cr# values in the range of 61–89%; Akmaz et al., 2014). Chrome from both chromititea and mantle peridotites of ophiolites are used as indicators of their tectonic setting of formation (Dick and Bullen, 1984; Kamenetsky et al., 2001; Arai et al., 2006). A general agreement has emerged that chromitites form in the depleted mantle section of ophiolites from the supra-subduction zone (SSZ) environments due to melt–rock or melt–melt interaction (Zhou et al., 1994, 1998; Ballhaus, 1998; Melcher et al., 1999; Uysal et al., 2005, 2007a,b,c; Rollinson and Adetunji, 2013). Arai and Miura (2015, 2016) reported that podiform chromitites form in a sub-arc magmatic setting and beneath mid-ocean ridges. According to these researchers, the Cr# of chromite of mid-ocean mantle peridotites is similar to that in the host harzburgite. This

is contrary to the observation that the Cr# of chromite is higher in chromitites than in host mantle peridotites in ordinary ophiolites or peridotite massifs. The Cr# of chromite of Tethyan ophiolites; such as Bulqiza, Eastern Mirdita ophiolite (Albania), Lycian, Pozantı-Karsantı, Kızıldağ, Guleman ophiolites (Turkey), Iran ophiolites, Northern Oman and Isabela-Philippines ophiolites have high Cr# of chromite (Bingöl, 1978; Xiong et al., 2015; Uysal et al., 2005; Akbulut et al., 2016; Chen et al., 2015; Shafaii Moghadam et al., 2015; Arai and Miura, 2015, 2016) are mostly high. According to the researchers Arai and Yurimoto (1994); González-Jiménez et al. (2014); Noller and Carter (1986) and Zhou et al. (1994), magma mixing is an essential factor for podiform chromitite formation in the mantle. It requires a harzburgite–melt reaction, so the chemical composition of the wall peridotite is very important (Arai, 1997; Arai and Abe, 1995). In a wall comprising highly refractory harzburgite containing chromite with Cr# >70%, the melt may have a high degree of chromite oversaturation (Arai, 1997). In this case, the chromitites contain chromite with high Cr# (Arai and Miura, 2015). The excess occurences of high Cr# chromite deposits indicate that the mantle wedge has been extremely depleted by partial melting. This extremely partial melting may occur in a forearc setting during subduction initiation (Stern et al., 2012).

Akbulut et al. (2016) studied major-, minor- and trace-element geochemistry of high-Cr chromites (ophiolitic podiform chromitites) from the Lycian and Antalya peridotites in southwestern Turkey and suggested a polygenetic origin from a range of arc-type melts within forearc and backarc settings. They also studied zircons in the chromitites and distinguished two types of zircons; (i) xenocrystic zircon, (ii) young zircon grains originating either from metasomatism of mantle peridotite or ocean crust recycled during subduction. According to them, the U–Pb age of 88 ± 1.6 Ma of young zircons dates the timing of its crystallization. This age remarkably coincides with the proposed timing of the intra-oceanic subduction and initiation of the contraction of the Neotethys Oceanic Basin (Akbulut et al., 2016). This age of subduction also coincides with the formation age of the Guleman ophiolite.

Beyarslan and Bingöl (2014) suggested that the Southeastern Anatolian ophiolites represent remnants of a Late Cretaceous oceanic forearc formed along the southern margin of Eurasia. The Guleman ophiolites and other southeast Taurus ophiolites are classic examples of Tethyan ophiolites that were obducted onto a passive continental margin and exposed by isostatic rebound of the continental margin beneath the ophiolites. Rifting between the Arabian Plate and Taurid Carbonate or Anatolian Plate to form the south branch of the Neo-Tethys Ocean began in the Late Triassic (Şengör and Yılmaz, 1981; Robertson, 2002). This Neo-Tethyan ocean basin persisted until the Late Cretaceous. The formation of the ophiolite above a northern dipping subduction zone began sometime in the Cretaceous (Beyarslan and Bingöl, 2014). Development of the Eastern Taurus ophiolites is shown schematically in Fig. 13.

Acknowledgements

This study was supported by a scientific research project from Firat University-Turkey (Project No. MF.13.05), and Institute of Earth Sciences, Academia Sinica, Taipei-Taiwan. We thank the authorities of these institutions. We wish to express our gratitude to reviewers of the Journal of African Earth Sciences for their comments, which greatly improved the manuscript.

References

Akbulut, M., González-Jiménez, J.M., Griffin, W.L., Belousova, E., O'Reilly, S.Y., McGowan, N., Pearson, N.J., 2016. Tracing ancient events in the lithospheric mantle: a case study from ophiolitic chromitites of SW Turkey. J. Asian Earth Sci. http://dx.doi.org/10.1016/j.jseaes.2016.01.008.

Akmaz, M., Uysal, I., Saka, S., 2014. Mineralogical and geochemical investigation of podiform chromitites from the Guleman ophiolite, eastern Turkey. Geophys. Abs. 16. EGU 2014-848-1.

Allan, J.F., 1994. Cr-spinel in depleted basalts from the Lau basin backarc: petrogenetic history from Mg–Fe crystal–liquid exchange. In: Hawkins, J., Parson, L., Allan, J.F., et al. (Eds.), Proceedings of the Ocean Drilling Program Scientific Results, vol. 135, pp. 565–583.

Anonymous, 1972. Penrose field conference on ophiolites. Geotimes 17, 24–25.

Arai, S., 1987. An estimation of the least depleted spinel peridotite on the basis of olivine- spinel mantle array. Neues Jahrb. für Mineral. Monatsh. 8, 347–435.

Arai, S., 1994a. Characterization of spinel peridotites by olivine–spinel compositional relationships: review and interpretation. Chem. Geol. 113, 191–204.

Arai, S., 1994b. Compositional variation of olivine–chromian spinel in Mg-rich magmas as a guide to their residual spinel peridotites. Volcanol. Geotherm. Res. 59.

Arai, S., 1997. Control of wall-rock composition on the formation of podiform chromitites as a result of magma/peridotite interaction. Resour. Geol. 47, 177–187.

Arai, S., Abe, N., 1995. Reaction of orthopyroxene in peridotite xenoliths with alkali basalt melt and its implications for genesis of alpine-type chromitite. Am. Mineral. 80, 1041–1047.

Arai, S., Miura, M., 2015. Podiform chromitites do form beneath mid-ocean ridges. Lithos 232, 143–149. http://dx.doi.org/10.1016/j.lithos.2015.06.015.

Arai, S., Miura, M., 2016. Reply to the comment of rollinson and adetunji "podiform chromitites do form beneath mid-ocean ridges" by Arai, S. and Miura, M. Lithos 254–255, 134–136.

Arai, S., Yurimoto, H., 1994. Podiform chromitites of the Tari-Misaka ultramafic complex, southwestern Japan, as mantle-melt interaction products. Econ. Geol. 89, 1279–1288.

Arai, S., Kadoshima, K., Morishita, T., 2006. Widespread arc-related melting in the mantle section of the northern oman ophiolite as inferred from detrital chromian spinels. J. Geol. Soc., Lond. 163, 869–879.

Ballhaus, C., 1998. Origin of podiform chromite deposits by magma mingling. Earth Planet. Sci. Lett. 156, 185–193.

Beyarslan, M., Bingöl, A.F., 2000. Petrology of a supra-subduction zone ophiolite (Kömürhan-Elazıg-Turkey). Can. J. Earth Sci. 37, 1411–1424.

Beyarslan, M., Bingöl, A.F., 2014. Petrology of the Ispendere, Kömürhan and Guleman ophiolites (southeast Turkey): subduction initiation rule (SIR) ophiolites and arc related magmatics. In: 3rd Annual International Conference on Geological and Earth Sciences, Proceedings, 22–23 September, Singapore.

Bingöl, A.F., 1978. Pétrologie du Masif Ophiolitique de Pozantı-Karsanti (Taurus Cilicien, Turquie): Etude de la Partie Orientale. Thése, Ph.D. Université Louis Pasteur, Strasbourg, France, 227 pp.

Bingöl, A.F., 1986. Petrographic and petrologique characteristic of the Guleman ophiolite (Eastern Taurus-Turkey). Gesound 13/14, 41–57.

Bingöl, A.F., Beyarslan, M., Chung, S.-L., 2014. The Peri-Arabian ophiolites (Turkey and Syria): mid-oceanic ridge (MOR) and/or subduction initiation rule (SIR) ophiolites. In: Proceedings XX Congress of the Carpathian-Balkan Geological Association, V.1, pp. 4–7. Tiran-Albania.

Bloomer, S.H., Fisher, R.L., 1987. Petrology and geochemistry of igneous rocks from the Tonga trench – a non-accreting plate boundary. J. Geol. 95, 469–495.

Bloomer, S.H., Hawkins, J.W., 1983. Gabbroic and ultramafic rocks from the Mariana trench: an island arc ophiolite. In: Hayes, D.E. (Ed.), The Tectonics and Geologic Evolution of Southeast Asian Seas and Islands: Part II, AGU Geophysical Monograph, vol. 23. American Geophysical Union, Washington, pp. 294–317.

Bonatti, E., Michael, P.J., 1989. Mantle peridotites from continental rifts to ocean basins to subduction zones. Earth Planet. Sci. Lett. 91, 297–311.

Boudier, F., Nicolas, A., Bouchez, J.L., 1982. Kinematics of oceanic thrusting and subduction from basal section of ophiolites. Nature 296, 825–828.

Casey, J.F., Dewey, J.F., 1984. Initiation of subduction zones along transform and accreting plate boundaries, triple-junction evolution, and forearc spreading centres Implications for ophiolitic geology and obduction. In: Gass, G., Lippard, S.J., Shelton, A.W. (Eds.), Ophiolites and Oceanic Lithosphere: Geological Society of London Special Publication, 13, pp. 269–290. http://dx.doi.org/10.1144/GSL.SP013.01.22.

Cassard, D., Nicolas, A., Rabinovitch, M., Moutte, J., Leblanc, M., Prinzhofer, A., 1981. Structural classification of chromite pods in southern New Caledonia. Econ. Geol. 76, 805–831.

Chen, C., Su, B.-X., Uysal, I., Avcı, E., Zhang, P.-F., Xiao, Y., He, Y.-S., 2015. Iron isotopic constraints on the origin of peridotite and chromitite in the Kızıldağ ophiolite, southern Turkey. Chem. Geol. 417, 115–124.

Choi, S.H., Shervais, J.W., Mukasa, S.B., 2008. Supra-subduction and abyssal mantle peridotites of the coast range ophiolite, California. Contrib. Mineral. Petrol. 156, 551–576.

Constantin, M., Hekinian, R., Ackermand, D., Stoffers, P., 1995. Mafic and ultramafic intrusions into upper mantle peridotites from fast spreading centers of the Easter Microplate (South East Pacific). In: Vissers, R.L.M., Nicolas, A. (Eds.), Mantle and Lower Crust Exposed in Oceanic Ridges and Ophiolites, pp. 71–120.

Dick, H.J.B., Bullen, T., 1984. Chromian spinel as a petrogenetic indicator in abyssal and alpian–type peridotites and spatially associated lavas. Contrib. Mineral. Petrol. 86, 54–76.

Dilek, Y., 2003. Ophiolite concept and its evolution. In: Dilek, Y., Newcomb, S. (Eds.), Ophiolite Concept and the Evolution of Geological Thought: Geological Society

of America Special Paper, 373, pp. 1–16.
Dilek, Y., Furnes, H., 2014. Ophiolites and Their Origins. Mineralogical Society of America, pp. 1811–5209. http://dx.doi.org/10.2113/gselements. 10.2.93.
Erdoğan, B., 1977. Geology, Geochemistry and Genesis of the Sulphide Deposits of the Ergani- Maden Region, Southeast Turkey. Ph.D. Thesis. Univ. of New Brunswick (unpublished).
González-Jiménez, J.M., Griffin, W.L., Proenza, J.A., Gervilla, F., O'Reilly, S.Y., Akbulut, M., Pearson, N.J., Arai, S., 2014. Chromitites in ophiolites: how, where, when, why? Part II. The crystallization of chromitites. Lithos 189, 140–158. http://dx.doi.org/10.1016/j.lithos.2013.09.008.
Hellebrand, E., Snow, J.E., Dick, H.J.B., Hoffmann, A.W., 2001. Coupled major and trace elements as indicators of the extent of melting in mid-ocean-ridge peridotites. Nature 410, 677–681.
Ishii, T., Robinson, P.T., Maekawa, H., Fiske, R., 1992. Petrological studies of peridotites from diapiric serpentinite seamounts in the Izu-Ogasawara-Mariana forearc, Leg 125. In: Fryer, P., Pearce, J.A., Stokking, L.B., et al. (Eds.), Proceedings of the Ocean Drilling Program Scientific Results, vol. 125, pp. 445–486.
Kamenetsky, V.S., Crawford, A.J., Meffre, S., 2001. Factors controlling chemistry of magmatic spinel: an empirical study of associated olivine, Cr-spinel and melt inclusions from primitive rocks. J. Petrol. 42, 655–671.
Karaoğlan, F., Parlak, O., Klötlz, U., Thöni, M., Koller, F., 2013. U-Pb ve Sm-Nd geochronology of the Kızıldağ (Hatay, Turkey) ophiolite: implication for the timing and duration of suprasubduction zone type oceanic crust formation in the southern Neotethys. Geol. Mag. 150/2, 238–299.
Lyubetskaya, T., Korenaga, J., 2007. Chemical composition of Earth's primitive mantle and its variance: 1. Methods Results J. Geophys. Res. 112, B03211. http://dx.doi.org/10.1029/2005JB004223.
Melcher, F., Grum, W., Simon, G., Thalhammer, T.V., Stumpfl, E.F., 1997. Petrogenesis of the giant ophiolitic chromite deposits of Kempirsai, Kazakhstan: a study of solid and fluid inclusions in chromite. J. Petrol. 38, 1419–1458.
Melcher, F., Grum, W., Thalhammer, T., Thalhammer, O., 1999. The giant chromite deposits at Kempirsai, Urals: constraints from trace element (PGE, REE) and isotope data. Mineral. Deposita 34, 250–272.
Metcalf, R.V., Shervais, J.W., 2008. Supra-subduction zone ophiolites: is there really an ophiolite conundrum?. In: Wright, J.E., Shervais, J.W. (Eds.), Ophiolites, Arcs, and Batholiths: Geological Society of America Special Paper, 438, pp. 191–222.
Milson, J., 2003. Forearc ophiolites: a view from the western Pacific. In: Dilek, Y., Robinson, P.T. (Eds.), Ophiolites in Earth History: the Geological Society of London Special Publications, 218, pp. 507–515.
Morishita, T., Dilek, Y., Shallo, M., Tamura, A., Arai, S., 2011. Insight into the uppermost mantle section of a maturing arc: the Eastern Mirdita ophiolite, Albania. Lithos 124, 215–226.
Niu, Y., 2004. Bulk-rock major and trace element compositions of abyssal peridotites: implications for mantle melting, melt extraction and post-melting processes beneath mid-ocean ridges. J. Petrol. 45 (12), 2423–2458.
Noller, J.S., Carter, B., 1986. The origin of various types of chromite schlieren in the Trinity Peridotite, Klamath Mountains, California. In: Carter, B., Chowdhury, M.K.R., Jankovic, S., Marakushev, A.A., Morten, L., Onikhimovsky, V.V., Raade, G., Rocci, G., Augustithis, S.S. (Eds.), Metallogeny of Basic and Ultrabasic Rocks (Regional Presentations). Theophrastus, Athens, pp. 151–178.
Özkan, Y.Z., Öztunalı, Ö., 1984. Petrology of the magmatic rocks of Guleman ophiolite. In: Proceeding of the International Symposium on the Geology of the Taurus Belt, pp. 285–293.
Özkaya, I., 1978. Ergani-maden Yöresi Stratigrafisi. Türk. Jeol. Kur. Bült. 21, 129–139.
Parkinson, I.J., Pearce, J.A., 1998. Peridotites from the Izu-Bonin-Mariana forearc (ODP Leg 125): evidence for mantle melting and melt–mantle interaction in a suprasubduction zone setting. J. Petrol. 39, 1577–1618.
Pearce, J.A., Lippard, S.J., Roberts, S., 1984. Characteristics and tectonic significance of suprasubduction zone ophiolites. In: Kokiaar, B.P., Howells, M.F. (Eds.), Marginal Basin Geology, vol. 16. Geological Society of London, pp. 77–94 (special publication).
Pearce, J.A., Vander Laan, S.R., Arculus, R.J., Murton, B.J., Ishii, T., Peate, D.W., Parkinson, I.J., 1992. Boninite and harzburgite from Leg 125 (Bonin-Mariana forearc): a case study of magma genesis during the initial stages of subduction. In: Fryer, P., et al. (Eds.), Proceeding of the Ocean Drilling Program, Scientific Results, Site 778–786, Bonin-Mariana Region. Ocean Drilling Program, College Station, Texas, pp. 623–659.
Pearce, J.A., Barker, P.F., Edwards, S.J., Parkinson, I.J., Leat, P.T., 2000. Geochemistry and tectonic significance of peridotites from the South Sandwich arc-basin system. South Atl. Contrib. Mineral. Petrol. 139, 36–53. http://dx.doi.org/10.1007/s004100050572.
Perinçek, D., 1979. The geology of Hazro-Korudağ Çüngüş-Maden-Ergani-Hazar-Elazığ-Malatya region. In: Guide book, Geological Society of Turkey, Special Publications, 33.
Perinçek, D., ve Çelikdemir, M.E., 1979. Geology and Petroleum Possibilities of Palu-Karabegan- Elazığ- Sivrice-malatya Region (unpublished). TPAO Arşivi. Rapor No: 1361.
Rigo de Righi, M., Cortesini, A., 1964. Gravity tectonics in foothills structure belt of Southeast Turkey. Amer. Petrol. Geol. Bull. 48 (12), 1911–1937.
Robertson, A.H.F., 2002. Overview of the genesis and emplacement of mesozoic ophiolites in the eastern mediterranean tethyan region. Lithos 65, 1–67.
Rollinson, H., Adetunji, J., 2013. Mantle podiform chromitites do not form beneath midocean ridges: a case study from the Moho transition zone of the Oman ophiolite. Lithos 177, 314–327.
Seyler, M., Lorand, J.P., Dick, H.J.B., Drouin, M., 2007. Pervasive melt percolation reactions in ultra-depleted refractory harzburgites at the Mid-Atlantic Ridge, 15°2′N: ODP hole 1274A. Contrib. Mineral. Petrol. 153, 303–319.
Shafaii Moghadam, H., Khedr, M.Z., Arai, Shoji, Stern, R.J., Ghorbani, G., Tamura, A., Ottley, Chris J., 2015. Arc-related harzburgite–dunite–chromitite complexes in the mantle section of the Sabzevar ophiolite, Iran: a model for formation of podiform chromitites. Gondwana Res. http://dx.doi.org/10.1016/j.gr.2013.09.007.
Shellnutt, J.G., Iizuka, Y., 2013. Chevkinite-group minerals from the mantle-derived metaluminous Woshui syenite of the Emeishan large igneous province. Eur. J. Mineral. 25, 671–682. http://dx.doi.org/10.1127/0935-1221/2013/0025-2309.
Shervais, J.W., 2000. Birth, death, and resurrection: the life cycle of supra subduction zone ophiolites. Geochem. Geophys. Geosystems 2.
Stern, R.J., Bloomer, S.H., 1992. Subduction zone infancy: examples from the Eocene Izu-Bonin-Mariana and Jurassic California arcs. Geol. Soc. Am. Bull. 104 (12), 1621–1636.
Stern, R.J., Reagan, M., Ishizuka, O., Ohara, Y., Whattam, S., 2012. To understand subduction initiation, study forearc crust; to understand forearc crust, study ophiolites. Lithosphere 4, 469–483.
Şengör, A.M.C., Yılmaz, Y., 1981. Tethyan evolution of Turkey, a plate tectonic approach. Tectonophysics 75, 181e241.
Uysal, I., Sadiklar, M., Tarkian, M., Karsli, O., Aydin, F., 2005. Mineralogy and composition of the chromitites and their platinum-group minerals from Ortaca (Muğla-SW Turkey): evidence for ophiolitic chromitite genesis. Mineral. Petrol. 83, 219–242.
Uysal, I., Zaccarini, F., Garuti, G., Meisel, T., Tarkian, M., Bernhardt, H.J., Sadiklar, M.B., 2007a. Ophiolitic chromitites from the Kahramanmaras area, southeastern Turkey: their platinum group elements (PGE) geochemistry, mineralogy and Os-isotope signature. Ofioliti 32, 151–161.
Uysal, I.M., Kaliwoda, M., Karsli, O., Tarkian, M., Sadiklar, M.B., Ottley, C.J., 2007b. Compositional variations as a result of partial melting and melt–peridotite interaction in an upper mantle section from the Ortaca area, southwestern Turkey. Can. Mineral. 45, 1471–1493.
Uysal, I.M., Tarkian, M., Sadiklar, M.B., Şen, C., 2007c. Platinum-group-element geochemistry and mineralogy of ophiolitic chromitites from the Kop mountains, Northeastern Turkey. Can. Mineral. 45, 355–377.
Üşümezsoy, Ş., 1986. Kefdağ ve Soridağ (Guleman) kromit kütlelerinim oluşumu üzerine yeni bir yaklaşım. Jeol. Mühendisliği 29, 47–60.
Whattam, S.A., Stern, R.J., 2011. The 'subduction initiation rule': a key for linking ophiolites, intra-oceanic forearcs and subduction. Contrib. Mineral. Petrol. http://dx.doi.org/10.1007/s00410-011-0638-z.
Xiong, F.H., Yang, J.S., Robinson, P.T., Xu, X.Z., Liu, Z., Li, Y., Li, J.Y., Chen, S.Y., 2015. Origin of podiform chromitite, a new model based on the Luobusa ophiolite, Tibet. Gondwana Res. http://dx.doi.org/10.1016/j.gr.2014.04.008.
Zhou, M.F., Robinson, P.T., Bai, W.J., 1994. Formation of podiform chromitites by melt/rock interaction in the upper mantle. Mineral. Deposita 29.
Zhou, M.-F., Robinson, P.T., Malpas, J., Li, Z., 1996. Podiform chromitites in the Luobusa ophiolite (southern Tibet): implications for melt-rock interaction and chromite segregation in the upper mantle. J. Petrol. 37, 3–21.
Zhou, M.F., Sun, M., Keays, R.R., Kerrich, R.W., 1998. Controls on platinum-group elemental distributions of podiform chromitites: a case study of high-Cr and high-Al chromitites from Chinese orogenic belts. Geochim. Cosmochim. Acta 62, 677–688.

Further reading

Hirose, K., Kawamoto, T., 1995. Hydrous partial melting of lherzolite at 1 Gpa: the effect of H_2O on the genesis of basaltic magmas. Earth Planet. Sci. Lett. 133, 463–473.